# e Prediction

# Rotordynamic Force Prediction of a Shrouded Centrifugal Pump Impeller—Part I: Numerical Analysis

# **Eunseok Kim**

Mem. ASME Department of Mechanical Engineering, Texas A&M University, College Station, TX 77840 e-mail: euns670@tamu.edu

# Alan Palazzolo

Fellow ASME
Department of Mechanical Engineering,
Texas A&M University,
College Station, TX 77840
e-mail: a-palazzolo@tamu.edu

Computational fluid dynamics (CFD) is employed to calculate the fluid-induced forces in the leakage path of an incompressible shrouded centrifugal impeller. Numerical solutions of the whirling shrouded impeller at the centered position provide the radial and tangential impedances that can be modeled as a quadratic function of whirl frequency. Calculated impedance results on a face-seal impeller can be modeled with a second-order function of whirl frequency and the predicted rotordynamic coefficients show reasonable agreement with the test results by Bolleter et al. (1989, "Hydraulic Interaction and Excitation Forces of High Head Pump Impellers," ôPumping Machinery: Third Joint ASCE/ ASME Mechanics Conference, La Jolla, CA, pp. 187–194). However, the present analysis shows that the calculated impedance curves for a conventional wear-ring seal impeller using three-dimensional (3D) numerical approach have "bumps" and "dips" which can be observed in the bulk flow analysis of impeller models by Childs (1989, "Fluid-Structure Interaction Forces at Pump Impeller-Shroud Surfaces for Rotordynamic Calculations," J. Vib., Acoust., Stress, Reliab. Des., 111(3), pp. 216–225). After reviewing previous predictions and experiments that showed the bump and dip in the computed and measured forces, the current study focuses on the estimation of the possible sources causing the peaks. The selected possible sources are inlet tangential velocity at the shroud entrance, flow rate of primary passage, shape of the shroud leakage path, and seal clearance. The fluid-induced forces of the conventional wear-ring seal impeller are calculated and analyses on the effects of these variables are provided. [DOI: 10.1115/1.4032722]

# 1 Introduction

Fluid-induced forces developed in the leakage flow path of a shrouded centrifugal pump and compressor impeller are possible sources that cause rotordynamic instability. Thus, understanding the mechanism of the forces is crucial to design stable machines and investigate the rotordynamic stability. In order to analyze these forces, much research has been performed to measure and predict the destabilizing forces on the secondary flow passage of the centrifugal impeller.

Jery et al. [1] measured radial and tangential forces of a 3D centrifugal impeller and the resulting impedances from the experiment fairly matched a quadratic curve. Least square curve fitting used to calculate the rotordynamic coefficients from the measured forces. The authors showed that the identified dynamic force matrix has equal diagonal elements and skew-symmetric off-diagonal elements. Bolleter et al. [2] tested a boiler feed pump impeller with vaned diffuser. Seal forces were not considered by employing a face seal on the suction side of the shrouded impeller. The rotordynamic coefficients of the impeller system were identified by performing hydrodynamic force measurements using translational motion and wide frequency range excitation. In 1989, Bolleter et al. [3] implemented additional experiments by changing the geometry of the impeller shroud, type of seal, spin speed, and temperature. The tested impellers had tighter clearance of the shroud leakage flow path and this resulted in higher values of the rotordynamic coefficients when compared to the results of Jery et al. [1]. In the test case of an impeller with an annular seal, a whirl frequency ratio (WFR) at instability was 2.26. The abnormally high value of the WFR at instability was reduced to 1.16 by attaching a small swirl break in the suction side of the impeller. Ohashi et al. [4] measured

Contributed by the Technical Committee on Vibration and Sound of ASME for publication in the JOURNAL OF VIBRATION AND ACOUSTICS. Manuscript received June 18, 2015; final manuscript received January 18, 2016; published online April 15, 2016. Assoc. Editor: John Yu.

lateral fluid forces on two- and three-dimensional centrifugal impellers. The authors evaluated the effect of vaned and vaneless diffusers, clearance between the front shroud and the casing, and interaction between the impeller and the guide vane. Yoshida and Tsujimoto [5] investigated the effect of the interaction between the impeller and the volute casing. The measured tangential force increased as the flow rate was reduced and the whirling speed lower. Tsujumoto et al. [6] implemented flow and pressure measurements in the back shroud/casing clearance of a precessing centrifugal impeller and integrated the unsteady pressure distribution to obtain the fluid moment coefficients.

Childs [7] employed a bulk flow analysis for the leakage path between an impeller shroud and a pump housing to predict rotordynamic coefficients. A face-seal pump impeller and a conventional wear-ring seal pump impeller were considered. In both cases, the calculated forces on the shroud surface showed peaks in the impedance curves. The calculated impedances for  $u_0(0) = 0.5$  could be modeled by a conventional linear model and the determined rotordynamic force coefficients showed reasonable correlation to experiment results measured by Bolleter et al. [2]. In Childs' model, recirculation zones in the shroud leakage path could not be captured since the bulk-flow model could analyze only one-dimensional fluid flow. To visualize the recirculation zones in the centrifugal impeller model, CFD techniques were used by several researchers. Baskharone et al. [8] modeled 3D eccentric impeller shroud region of Sulzer impeller and evaluated the rotordynamic coefficients using finite element method (FEM)-based solution. In 1999, Baskharone and Wyman [9] investigated the main and leakage flow by adding the primary passage on the centrifugal impeller. Moore and Palazzolo [10] performed prediction of the rotordynamic forces arising from the secondary flow passage of the shrouded centrifugal impeller using TASCflow, which is a commercial code utilizing finite volume method (FVM)-based CFD technique.

Gupta and Childs [11] utilized a bulk flow model for compressible flow and provided reasonable results. The incompressible bulk

flow model showed dips and bumps in the calculated impedance curves and the recirculation zones did not appear due to the limitation of the bulk flow model. Moore et al. [12] adopted a commercial CFD code for predicting the rotordynamic coefficients of a centrifugal compressor and suggested a new analytical formula for predicting the cross-coupled stiffness for the centrifugal impellers by a parametric study.

The above references mainly utilized a quadratic impedance curve assumption yielding mass, stiffness, and damping coefficients. The 3D CFD solutions for a face-seal centrifugal impeller did not show evidence of bumps and dips in the predicted impedance curves. However, some experimental results showed unconventional impedances that could not be described by the quadratic fit force model. Franz and Arndt [13] tested impeller/volute combinations to identify the hydrodynamic forces in the shroud region and measured nonquadratic impedance curves at decreased flow rate in the research. Brennen et al. [14] also observed the bump and dip in the measured radial and tangential forces of the centrifugal impellers at lower flow operations. Similar experimental evidences were observed in Figs. 8 and 9 of Bolleter et al. [3]. He pointed out that the measured plots of radial and tangential impedances did not have parabola curves at lower flow rates in the paper.

In this paper, CFD will be utilized to evaluate the fluid induced, dynamic forces arising in the leakage flow path of the shrouded centrifugal impeller. The face-seal impeller case is investigated and comparison is made with previous results in the literature to validate the approach of the present study.

The conventional wear-ring seal pump impeller is modeled while varying parameters such as inlet swirl ratio (ISR:  $V_0/\omega$ ) at shroud inlet, end seal clearance, flow rate of primary passage, and shape of shroud. The results are analyzed and compared with selected centrifugal impeller experiments in the literature. The CFD results replicate the nonquadratic behavior appearing in test results and in the bulk flow model of Childs.

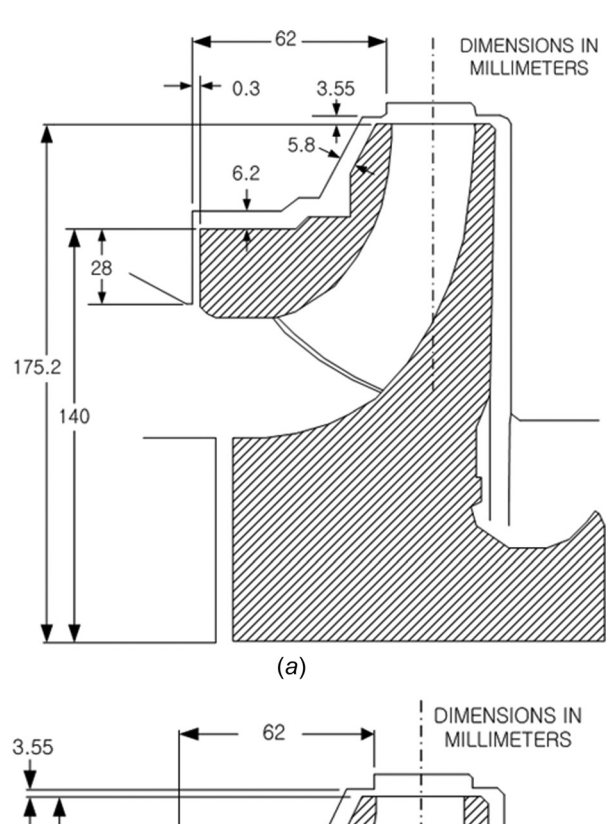
# 2 Numerical Method Description

**2.1** Computational Model and Mesh. The present study utilizes ansys cfx to predict the rotordynamic impedances induced by fluid forces on the shroud surface and to calculate rotordynamic coefficients of the shrouded centrifugal impeller. The commercial CFD program, ansys cfx, adopts an element-based FVM to discretize Navier–Stokes equations. A high-resolution scheme is applied as a discretization method and standard k– $\epsilon$  turbulence model with scalable log wall function is selected to calculate the fluid-induced forces of shrouded centrifugal impellers. The detailed theory for the numerical analysis in this paper is explained in Ref. [15].

Figure 1 shows geometric and dimensional information for the face-seal impeller and a conventional wear-ring seal impeller, which is used for the CFD simulations. Dimensions in each impeller model are indicated based on the information in Refs. [7,10]. In case of the face-seal impeller, some of the dimensions of the leakage flow path in the shroud model had to be approximated because the exact geometry information is unclear in the references.

The 3D shroud only models with circular whirl orbit are constructed first and the corresponding 3D eccentric grids of those models are then generated as shown in Fig. 2, in order to calculate the rotordynamic impedances and coefficients for the selected impeller models. ANSYS ICEM CFD is utilized to construct the 3D body fitted hexahedral meshes. The imposed circular whirl orbit radius value is determined as 10% of the shroud clearance based on Ref. [16].

**2.2 Boundary Conditions.** The impeller models are composed of three domains as shown Fig. 2. The diffuser domain in each numerical model is added to impose the inlet swirl velocity on the secondary flow path, which can be set in the computational model by defining the domain as a rotating frame. Two surfaces located between domains are set as domain interfaces to define



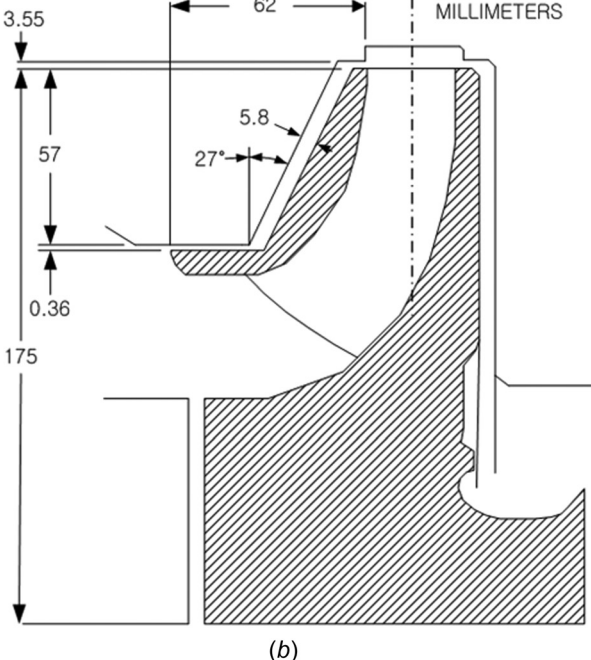
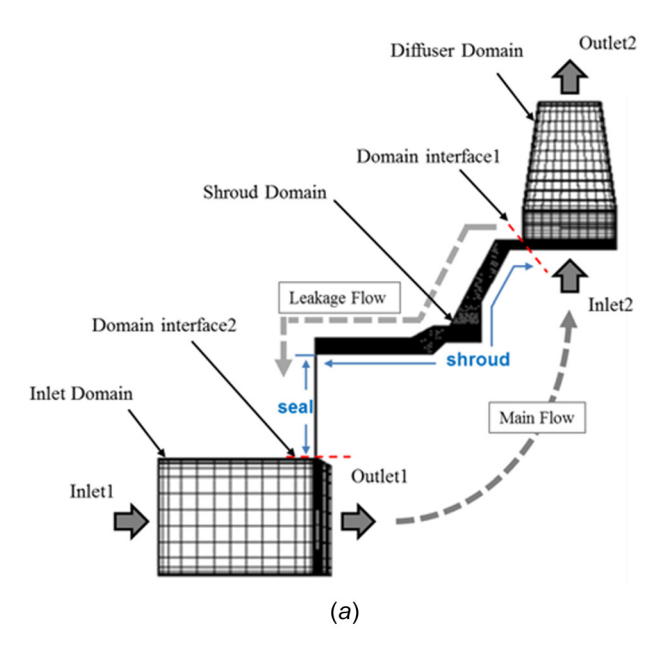


Fig. 1 Nominal configuration of impeller (a) face-seal impeller and (b) wear-ring seal impeller [7]

domains rotating at different spin rates. The numerical impeller models have two inlets and two outlets and they are placed in the diffuser and inlet domains as shown in Fig. 2. The same mass flow rate should be imposed at the two inlets since the omitted primary flow passage is a continuous flow path. The outlet pressures are determined based on the head rise at the main flow region. Based on the operating conditions provided in the research of Bolleter et al. [2], the boundary conditions at  $\Omega=0$  are specified as shown in Table 1, where  $\Omega$  is the whirl velocity as shown in Fig. 3. Stationary walls in the rotating frames are treated as counter-rotating walls and a no-slip condition is imposed at all walls in the numerical model. For the numerical calculation, a 64-bit processor with four cores operating at 28 GHz and 8 GB memory are utilized and the desired convergence target of each solution is  $10^{-4}$  or an even lower value.



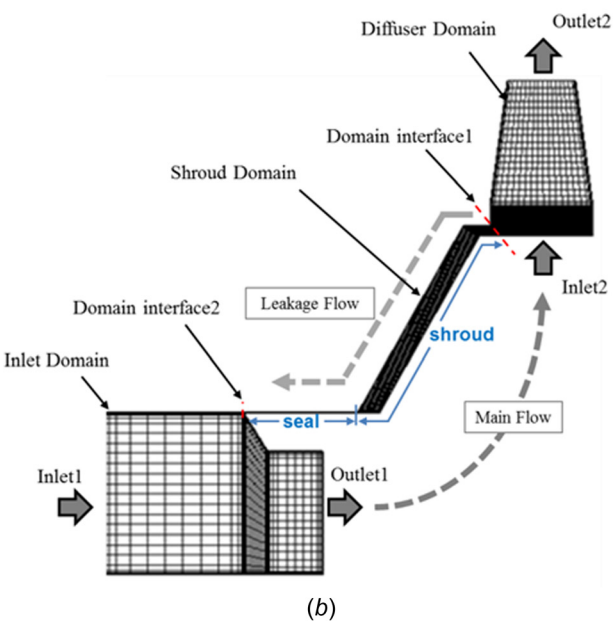


Fig. 2 Cut plane view of 3D eccentric grid (a) face-seal impeller and (b) wear-ring seal impeller

Table 1 Boundary conditions for the shrouded impeller model at  $\Omega = 0$ 

Parameters	Values		
Working fluid	Water		
Fluid temperature	26.5 deg		
Inlet swirl ratio	0.5		
Flow rate at inlet 1	130 kg/s		
Flow rate at inlet 2	130 kg/s		
Static pressure at outlet 1	0.1 MPa		
Static pressure at outlet 2	0.57 MPa		
Stationary walls	Treat as a counter rotating wall		
Rotating walls	2000 rpm		

2.3 Calculation of Rotordynamic Coefficients. Figure 3 illustrates the whirling motion of the rotor utilized in the present study. The points O and p indicate the center of the whirling orbit and the center of the impeller, respectively. The distance  $\varepsilon$ 

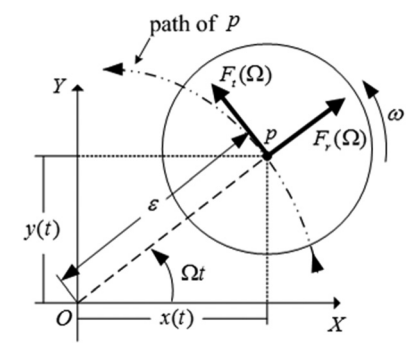


Fig. 3 Circular whirl orbit motion of the impeller

represents the whirl orbit radius of the impeller. The shrouded impeller is whirling at the angular rate  $\Omega$ , while the shroud surface spins about the center of the rotor at the spin rate  $\omega$ .

At  $\Omega t = 0$  in Fig. 3, the radial and tangential forces (per whirl radius) exerted on the impeller are expressed as

$$\frac{F_r}{\varepsilon} = -K - c\Omega + M\Omega^2$$

$$\frac{F_t}{\varepsilon} = k - C\Omega - m\Omega^2$$
(1)

Calculating the rotordynamic coefficients of Eq. (1) using the CFD technique has been widely studied and used for various types of seals [17] and impellers [10,12] in the past. A similar approach is utilized here for the numerical solution process to obtain the rotor-dynamic coefficients over a wide whirl frequency range, for use in both imbalance response and rotordynamic stability simulations.

# 3 Rotordynamic Analysis on Shrouded Centrifugal Impeller

**3.1 Face-Seal Impeller Shroud.** The 3D eccentric grid model of the face-seal impeller does not include the primary passage as shown in Fig. 2(a) because the exact geometry information of the impeller blade is unavailable. Thus, the 3D shroud only model which was utilized in the previous CFD research [8,10] is used to determine the rotordynamic coefficients. In addition, the entrance and the elbow region of the shroud leakage path also have to be approximated because of the lack of geometry information.

Three grid models (coarse, medium, and fine) are constructed to determine the appropriate mesh size for the rotordynamic predictions. The sizes of the coarse, medium, and fine mesh are  $0.46 \times 10^{6}$ ,  $0.82 \times 10^{6}$ , and  $1.61 \times 10^{6}$  nodes, respectively. Figure 4 shows the predicted impedances for the three grid models. The results of the medium grid and the fine grid model are almost identical and the coarse grid result has negligible differences from other grid models. Moreover, when considering the fact that a grid model with 187,800 nodes in the previous study [10] could predict reliable solutions for the face-seal impeller case, the fine grid can be considered enough to determine the fluid induced forces. A wide range of WFRs (WFR,  $f = \Omega/\omega$ ) is investigated in the mesh density study to check the existence of the bump and dip which were observed in the bulk flow analysis by Childs [7]. Slight bump and dip are observed in the CFD calculated impedances in Fig. 4. In this case, the computed results can be reasonably curve fit to Eq. (1), to obtain the rotordynamic coefficients because the magnitudes of the bump and dip are small enough to ignore. The predicted results are compared to the results of previous studies in Table 2. The calculated direct and cross-coupled stiffness are underpredicted and the direct damping is somewhat overpredicted when compared to the experiment results. However, when considering the fact that geometry approximations had to be made for constructing the current face-seal impeller model, the overall results show reasonable agreement with the experimental data.

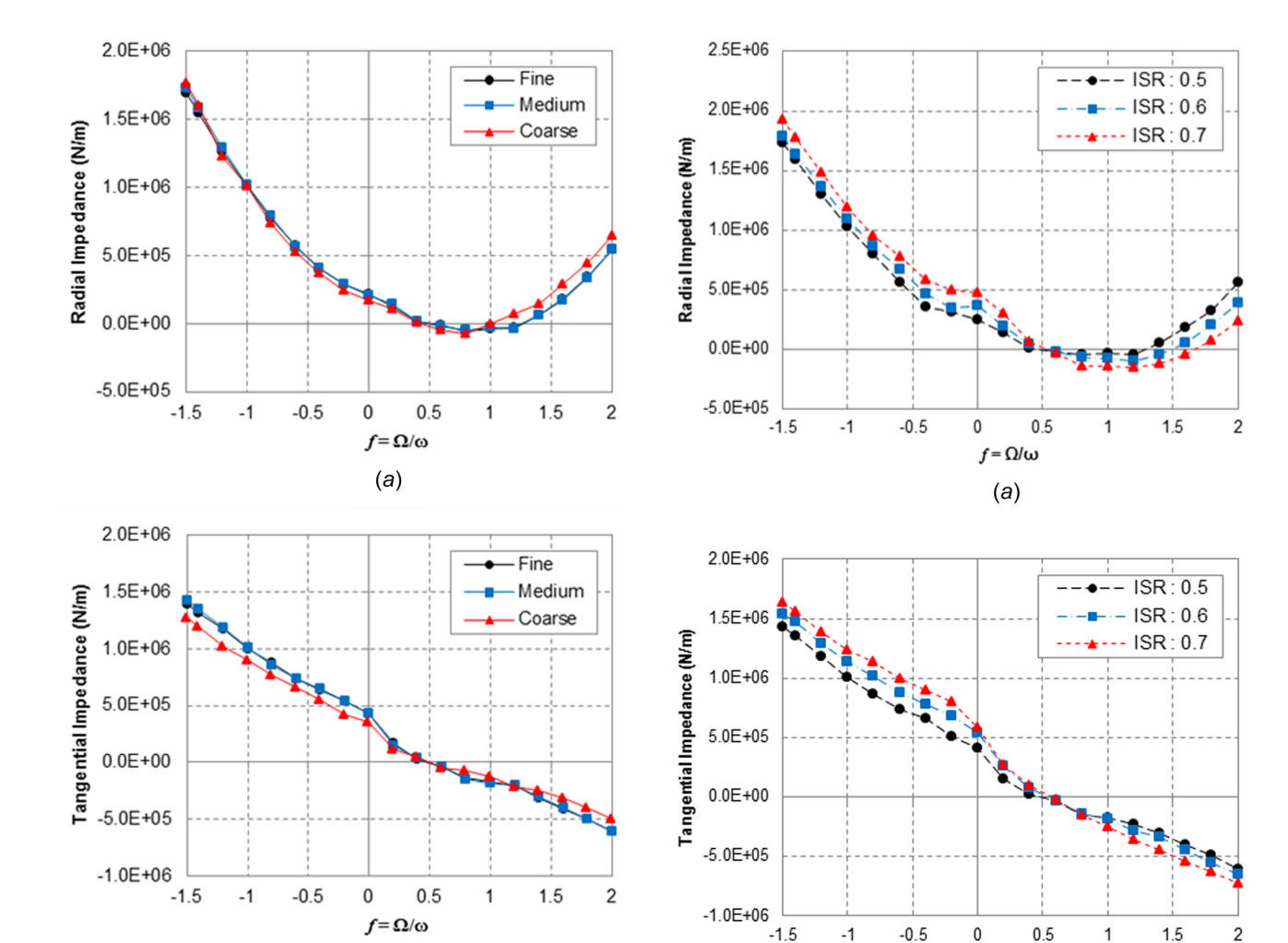


Fig. 4 Influence of grid density on impedance curves of faceseal impeller (a) radial and (b) tangential

(b)

The effect of the ISR on the face-seal impeller is investigated in Fig. 5 to determine its influence on the impedance curves. The *y*-intercepts of the impedance curves are increasing and therefore by Eq. (1) the absolute values of the direct and cross-coupled stiffness are increasing as the intensity of the inlet swirl at the shroud entrance becomes larger. Small deviations from the forms in Eq. (1) can be seen and their magnitudes are increasing at higher ISR. However, the magnitudes of the bump and dip are smaller than the results of Childs [7] and the shapes of the peaks are quite different.

# 3.2 Conventional Wear-Ring Seal Impeller

3.2.1 Mesh Density Study for Conventional Wear-Ring Seal Impeller. In this section, a mesh density study is performed to obtain reliable results and determine optimal grid model for the calculation of the impeller reaction forces. Table 3 shows the grid

Fig. 5 Impedances for the face-seal impeller according to ISR (a) radial and (b) tangential

 $f = \Omega/\omega$ 

(b)

Table 3 Comparison of grid models of the wearing seal impeller

Grid model	No. of nodes	Calculation time for WFR = 0
Fine	1,949,568	$5.123 \times 10^3 \mathrm{s}$
Medium	1,310,836	$3.827 \times 10^{3} \text{ s}$
Coarse 1	810,768	$2.640 \times 10^{3} \text{ s}$
Coarse 2	224,200	$8.722 \times 10^2 \mathrm{s}$
Coarse 3	159,488	$6.942 \times 10^2 \mathrm{s}$

models for the mesh density study and the corresponding calculation time per WFR. The grid model is defined as a coarse grid in cases of less than a million nodes. CFD calculations are implemented and the leakage flow rates are compared in Fig. 6. As

Table 2 Calculated rotordynamic coefficients for the face-seal shrouded impeller

	K (N/m)	c (N s/m)	M (kg)	k (N/m)	C (N s/m)	m (kg)
Present model FVM [10] Experiment [3] FEM [8] Bulk flow model [7]	$-2.50 \times 10^{5}$ $-3.24 \times 10^{5}$ $-3.53 \times 10^{5}$ $-2.68 \times 10^{5}$ $-4.20 \times 10^{4}$	$3.58 \times 10^{3}$ $3.59 \times 10^{3}$ $6.80 \times 10^{3}$ $2.92 \times 10^{3}$ $2.29 \times 10^{3}$	$1.01 \times 10^{1}$ $7.92 \times 10^{0}$ $2.36 \times 10^{1}$ $5.03 \times 10^{0}$ $8.96 \times 10^{0}$	$4.10 \times 10^{5}$ $4.71 \times 10^{5}$ $5.06 \times 10^{5}$ $1.65 \times 10^{5}$ $2.88 \times 10^{5}$	$4.35 \times 10^{3}$ $4.05 \times 10^{3}$ $2.58 \times 10^{3}$ $1.64 \times 10^{3}$ $2.02 \times 10^{3}$	$-6.06 \times 10^{0}$ $-2.92 \times 10^{0}$ $8.85 \times 10^{0}$ $3.03 \times 10^{0}$ $-9.00 \times 10^{-3}$

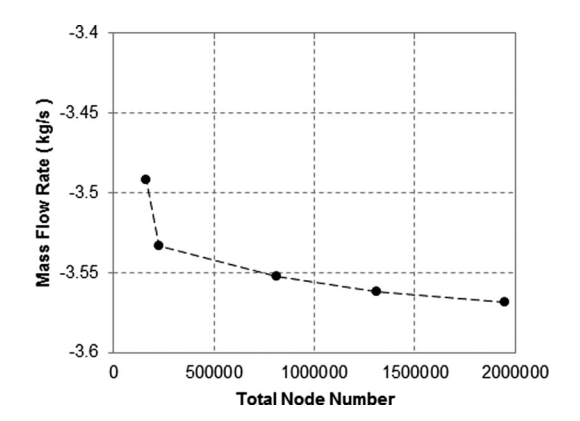
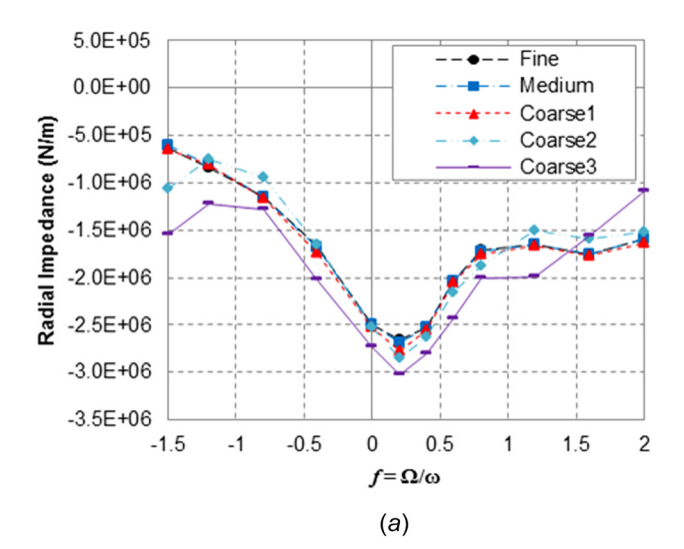


Fig. 6 Leakage flow rate at seal outlet of the wear-ring seal impeller according to the total node number



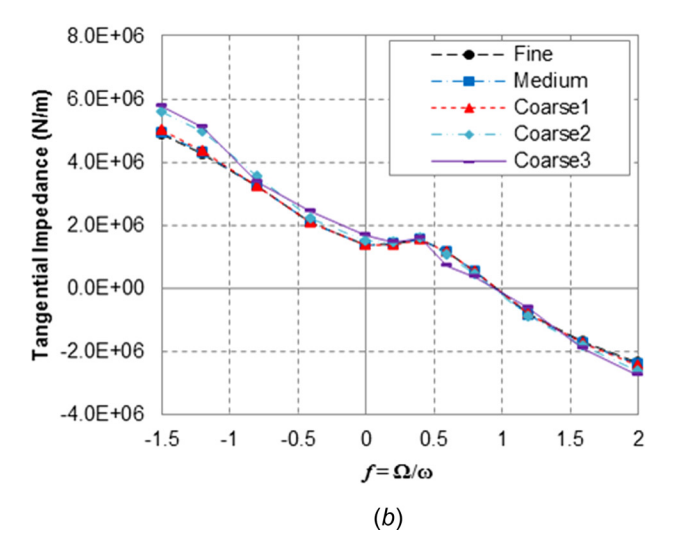


Fig. 7 Influence of grid density on impedance curves of the wear-ring seal impeller (a) radial and (b) tangential

shown in the figure, no noticeable changes are observed for the grid models over 800,000 nodes and the difference between the medium and fine grid is only 0.5%. Fig. 7 shows a comparison of the impedances for the various grid models. In cases of coarse 2 and coarse 3, the calculated impedances have some significant differences when compared to the other cases. The results of the

medium and fine grid are almost identical. Based on the results, the CFD solutions for the fine grid can be considered as converged results and therefore the fine grid model is selected for the simulation in this paper.

3.2.2 CFD Analysis for Conventional Wear-Ring Seal Impeller. Figure 2(b) shows the 3D eccentric grid of the conventional wear-ring seal impeller. This model is also constructed without blade region and has three domains like the face-seal impeller case. And the detailed boundary conditions used for the numerical simulation of the conventional wear-ring seal are the exactly those of the face-seal impeller case. The shroud domain of the wear-ring seal impeller is divided into two sections: seal and shroud as shown in Fig. 2(b), in order to evaluate the fluid induced forces on the seal and shroud surface separately. Figures 8 and 9 show the predicted radial and tangential impedances of combined (seal + shroud), shroud, and seal versus the WFR, which ranges from -1.5 to 2.0. The radial and tangential impedances in the figures have the dip and bump shapes in the frequency ratio range 0-0.5. The predicted impedance curves for the shroud of the wear-ring seal impeller in Figs. 8(b) and 9(b) have similar trends with the bulk flow results of Childs [7]. The peaks are clearly present in the computed curves and the magnitudes of the bump and dip are increasing at higher ISR. Figures 8(c) and 9(c) indicate the computed radial and tangential impedances for the wear-ring seal of the impeller model. The seal results show relatively small bump and dip when compared to the values of the shroud. In case of the tangential impedance, the fluid induced forces on the shroud contribute most for generating the bump in the curves. Generally, the x-intercept of the tangential impedance curve can be defined as the WFR at instability,  $\Omega_w = k/C\omega$ , if the curve is approximately linear. With higher  $\Omega_w$ , the impeller is more destabilizing. In Fig. 9(a), the x-intercept of the tangential impedance has a higher value for increased ISR and thus it can be concluded that the impeller tends to be more destabilizing at higher ISR. The same phenomenon could be observed in the results of the bulk flow analysis by Childs [7].

The peaks in the impedance curves of the centrifugal impeller could be also observed clearly in the past experimental results from the Caltech program by Franz and Arndt [13] as shown in Fig. 10. In that paper, the tangential and radial impedances of centrifugal impeller had been measured by varying the flow rate of the primary passage with constant speed and the several types of volutes and impellers. They investigated the influence of the flow rate on the rotordynamic instability and concluded that the volute had impact on the hydrodynamic force for high flow rates and the shape of the tangential force curve and the destabilizing force were affected by the flow rate. The same phenomenon was observed in the experiment by Brennen et al. [14]. In their research, the bump and dip were also shown in the measured forces at low flow coefficients and the authors concluded that the impedance bump and dip were independent of volute type.

3.2.3 Effect of Main Flow Rate. Figure 11 illustrates the measured tangential forces at three different flow coefficients by Franz and Arndt [13]. As discussed previously, they evaluated the effect of flow coefficients and found that the shape of the force curves was influenced by the flow coefficients. In this section, a 3D numerical model of the conventional wear-ring seal impeller is employed to determine the dependence of impedances on flow rate through the primary passage. The flow rates of the primary passage are used as inlet boundary conditions for the numerical solutions of the face-seal impeller and the conventional wear-ring seal impeller in the present study. The boundary conditions are indicated in Table 1. In order to evaluate the effect of the flow rate on the wear-ring seal impeller, the flow rates on inlet boundary conditions are changed. The flow rate is changed from 130 kg/ s to 250 kg/s and 300 kg/s. Note that the static pressures are assumed to be constant for the cases. Figure 12 shows the computed impedance curves according to the flow rate in the primary

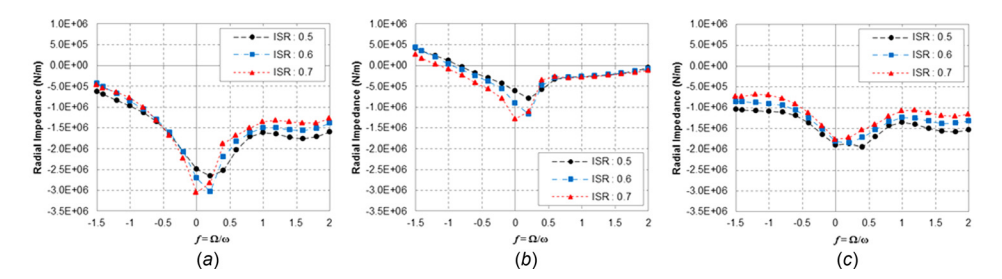


Fig. 8 Radial impedances for the wear-ring seal impeller according to the ISR (a) combined (shroud + seal), (b) shroud, and (c) seal

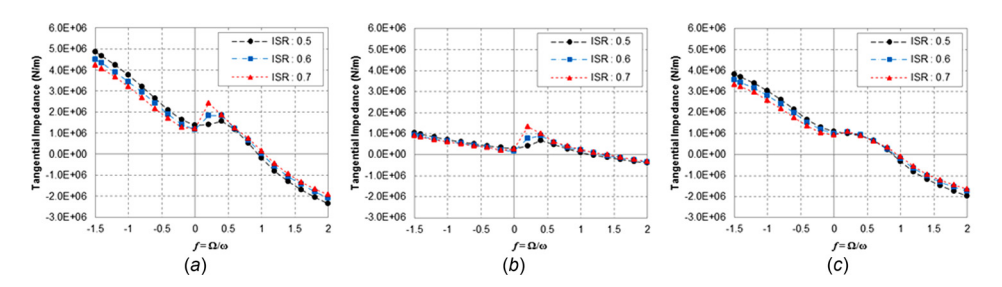
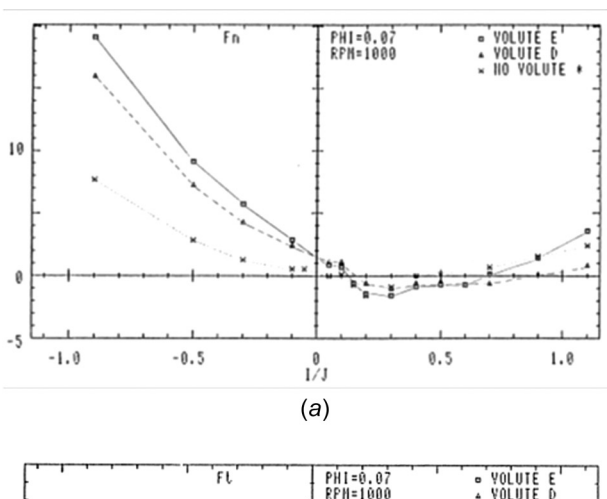


Fig. 9 Tangential impedances for the wear-ring seal impeller according to the ISR (a) combined (shroud + seal), (b) shroud, and (c) seal



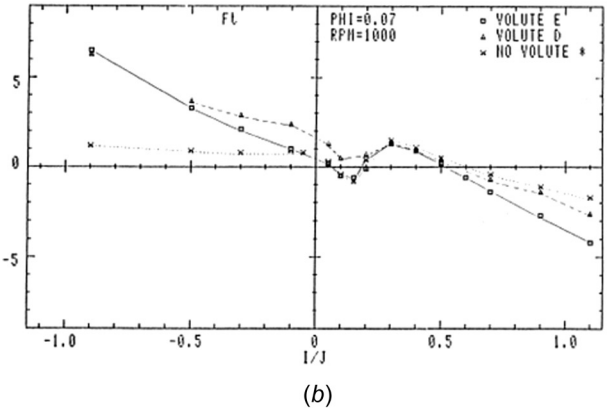


Fig. 10 Averaged forces measured by Franz and Arndt [13] (a) radial and (b) tangential

passage. In the results, it is observed that as the main flow rate increases, the shape of the bump and dip in the impedance curves changes. In case of the radial impedance in Fig. 12(a), the magnitude of the bump in the curve becomes smaller with lowered flow

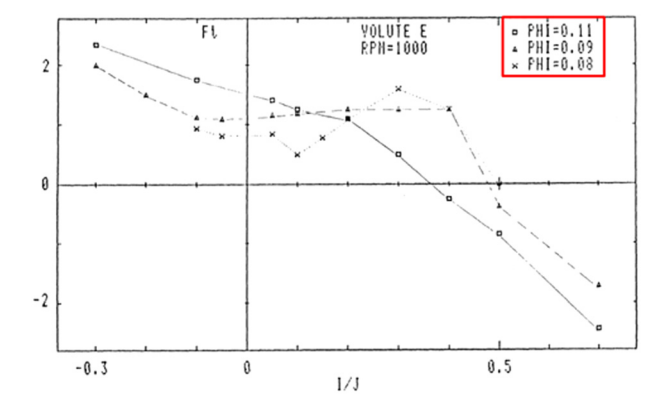


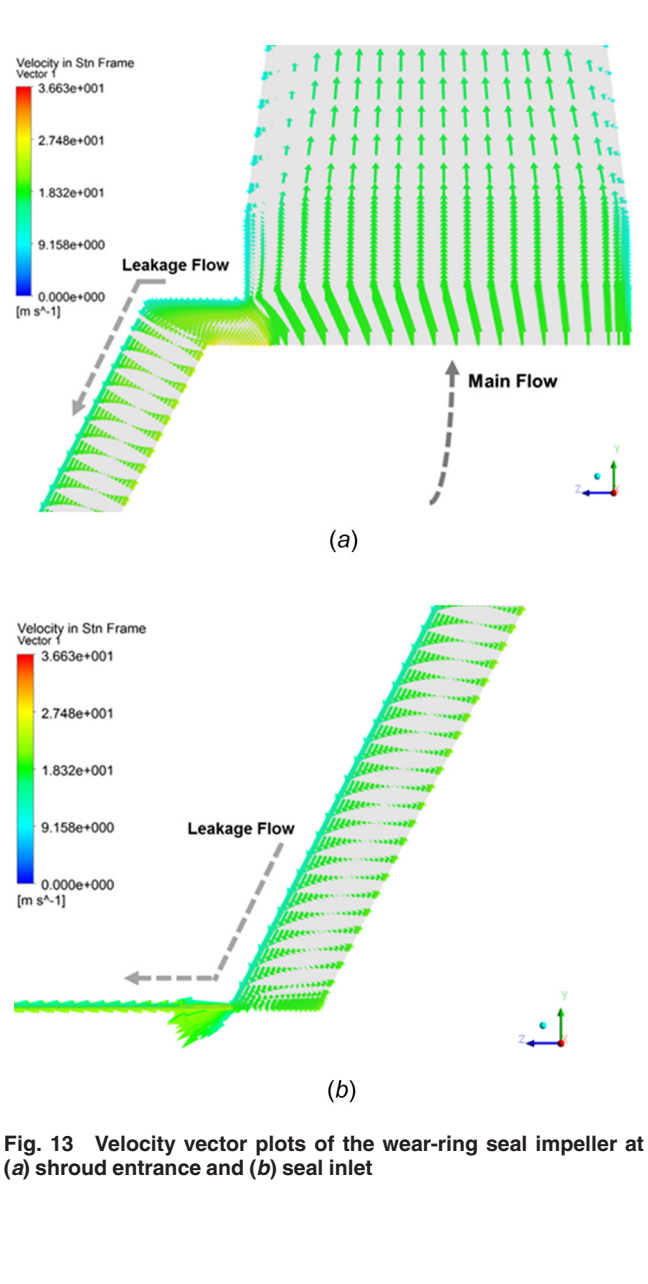
Fig. 11 Measured tangential forces according to the flow rate by Franz and Arndt [13]

rate. Figure 12(b) describes the computed tangential impedances according to the flow rate. At the highest flow rate, the y-intercept of the tangential impedance has the largest value and the x-intercept has the smallest value. This tendency of the current numerical solution is identical to the measured data in Fig. 11 and it can be concluded that the wear-ring seal impeller is viewed as being less destabilizing at lower flow rate.

3.2.4 Effect of Shroud Leakage Path Shape. Childs [7] explained that the bump and dip in the impedance curves computed by the bulk flow analysis appear because of a centrifugal acceleration term in the path-momentum equation. He explained that the peaks substantially decreased when the term was removed in the path-momentum equation of the bulk flow model. The bulk flow centrifugal acceleration term was defined as follows:

$$\frac{2u_{\theta 0}}{r}\frac{dr}{ds}/b^2\tag{2}$$

where  $u_{\theta\theta}$  is the circumferential velocity, and r, s, and b are the nondimensional variables of the inlet radius, path length, and velocity ratio in Ref. [7]. The centrifugal acceleration effect in the shroud region is visualized in the vector plot near the shroud



wnloaded from http://asmedigitalcollection.asme.org/vibrationaccoustics/article-pdf/138/3031014/6346637/vib\_138\_03\_031014.pdf?casa\_token=orjJsTiujzQAAAAA:Yg0eBEhCe4a-EAu3llHAao-0\VZAetusZxDnEVhlABx2\Vx89oRoV9qemrUG1\_C-U2w0xMnUb by Texas A & M University user on 08 August 20

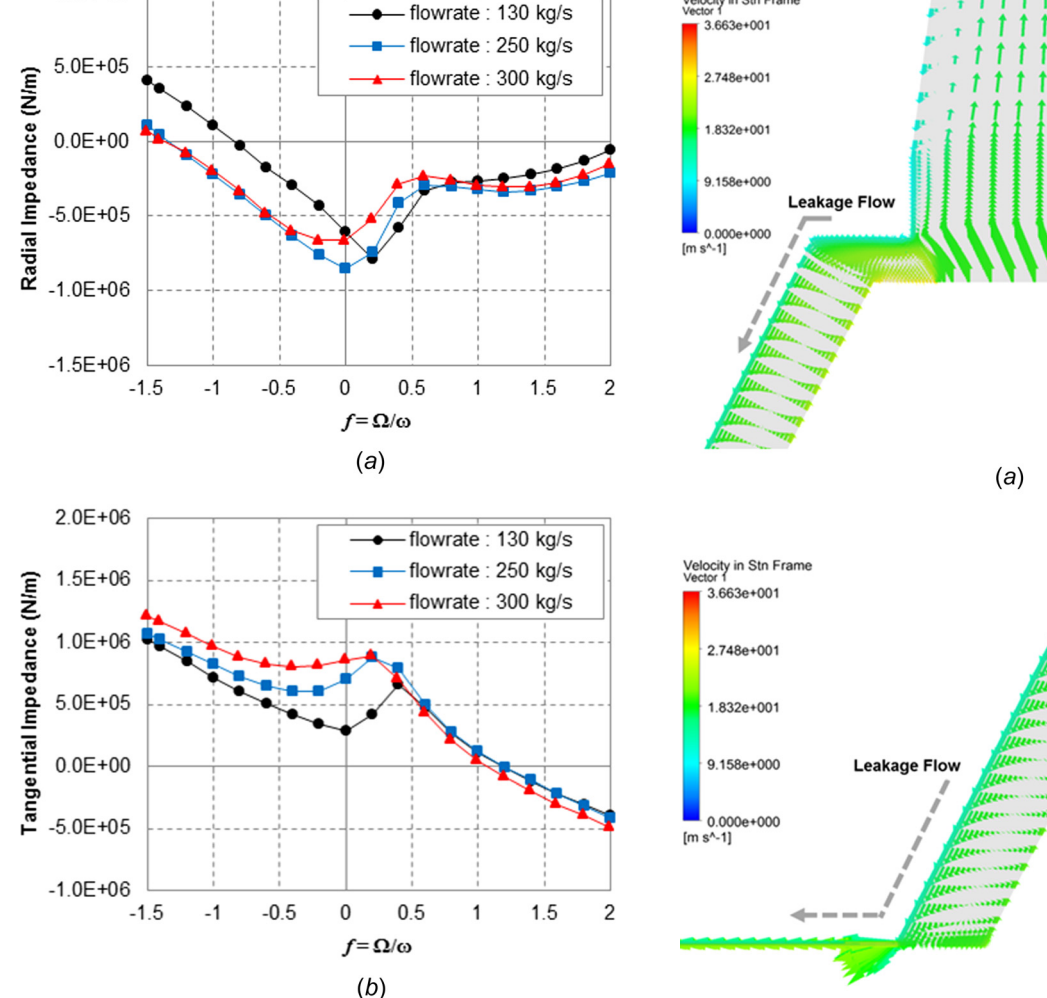


Fig. 12 Impedances on the shroud for three flow rates of the primary passage (a) radial and (b) tangential

1.0E+06

surface as indicated in Fig. 13. In Figs. 13(a) and 13(b), the fluid flow near the shroud surface of the impeller is pushed up while the fluid near the stator wall flows to downward due to the pressure difference between the shroud entrance and the outlet of the wear-ring seal.

In Eq. (2), the circumferential velocity term is one of the factors that has an influence on the centrifugal acceleration. Thus, reducing the velocity near the shroud wall can make the centrifugal acceleration decrease. In order to reduce the velocity of the reverse flow near the shroud surface, the geometry of the shroud region is changed as illustrated in Fig. 14. Additional recirculation zones are added by assuming that strong recirculation in the shroud region can slow down the velocity of the reverse flow and circumferential velocity. Three cases referred to as A1, A2, and A3 are considered to evaluate the effect of the added zone on the impedance curves of the wear-ring seal impeller model. The widths and heights of the cases are shown in Table 4. CFD models are constructed and the flow fields of the models are calculated using these parameter values. Figure 15 shows the recirculation flow in the added zone (A2). The averaged circumferential velocity along the z-axis of the entire shroud region is obtained for the changed shroud cases and the original shroud case. The sampled region to obtain the averaged circumferential velocity for all compared cases is indicated in Fig. 14. A comparison of the averaged circumferential velocity is made in Fig. 16. The averaged circumferential velocity in the shroud region decreases as the area of the added zone increases. Since the clearance near to the shroud

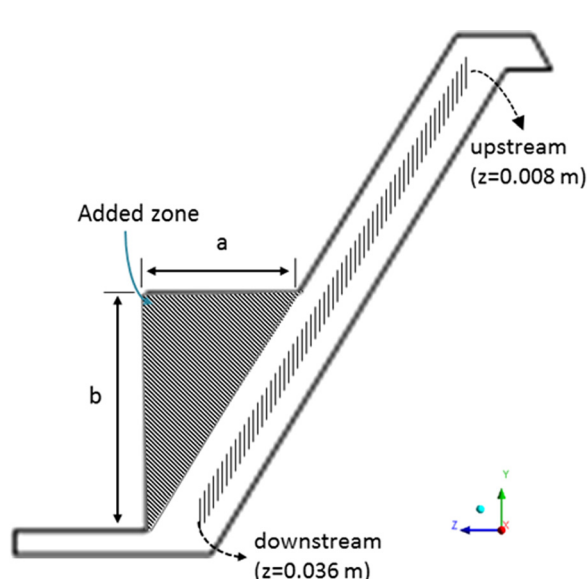


Fig. 14 Modified shroud geometry on stator-side

	A1	A2	A3
a (mm)	10.2	15.3	20.4
b (mm)	20.0	30.0	40.0

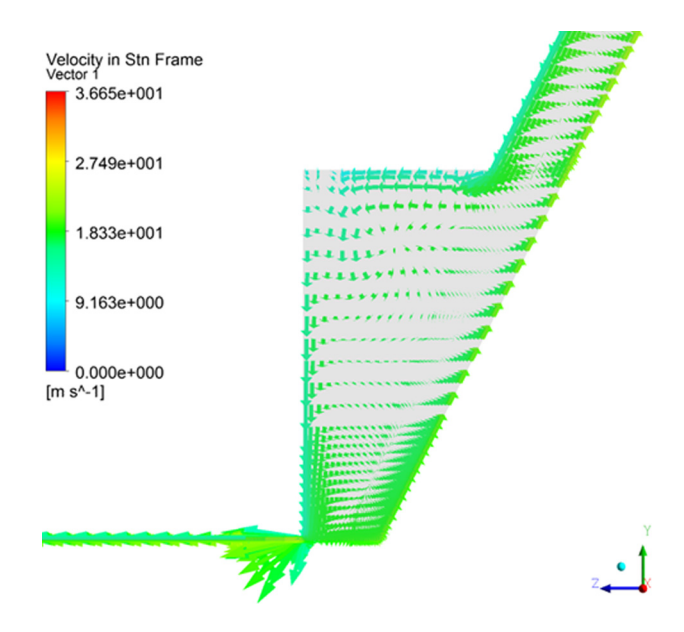


Fig. 15 Vector plots in the added recirculation zone (A2)

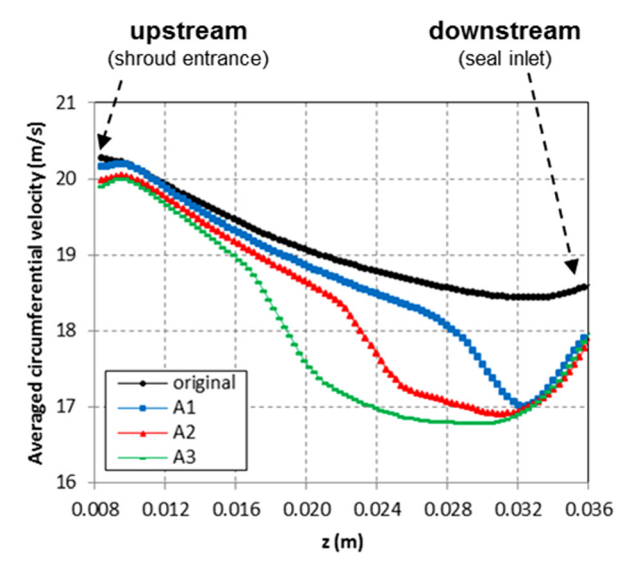
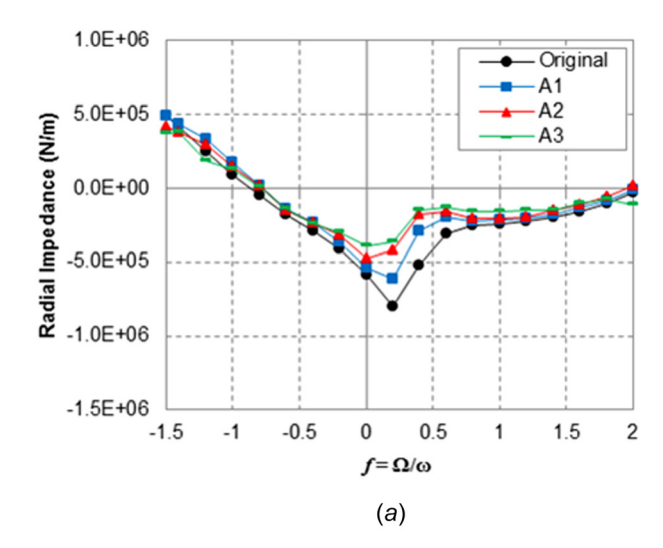


Fig. 16 Averaged circumferential velocity according to the shape of shroud

entrance is same, the effect of the added area is relatively small and therefore the velocity differences of all the cases could be considered negligible. However, the velocity differences around the enlarged shroud zone are large enough to have an influence on the shear stress on the shroud surface. In order to check the effect of the added zone on the shroud leakage path, the radial and tangential impedances of the shroud are compared according to the size of the added zone including the original wear-ring seal impeller model in Fig. 17. Adding the recirculation zone reduces the magnitude of the bump and dip in the impedance curves and the



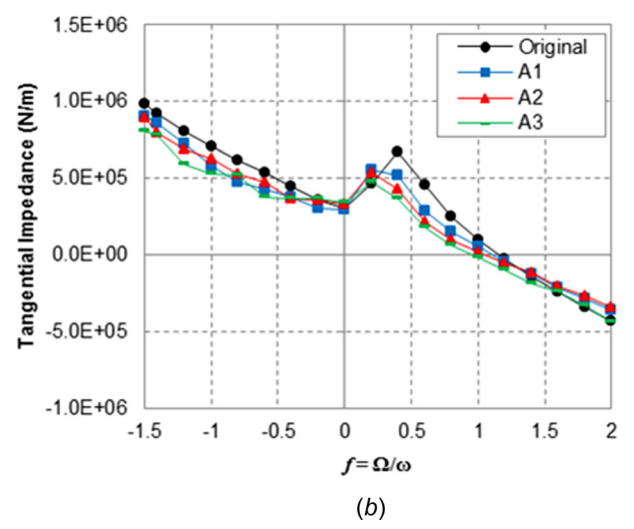


Fig. 17 Impedances on the shroud according to the secondary flow path geometry (a) radial and (b) tangential

Table 5 Comparison of leakage flow rate according to the size of the added zones

	Added zone			
	Original	A1	A2	A3
Leakage (kg/s)	3.5685	3.2350	3.2344	3.2549

cross-coupled stiffness. Increasing the area in the shroud region further reduces the peaks in the impedance curves. Reducing the velocity in the leakage flow path is effective for decreasing the peaks from the impedance predictions and modifying the shroud shape is one possible solution to reduce the circumferential velocity and centrifugal acceleration. The leakage flow rate is reduced by about 10% when the additional recirculation zone is added as indicated in Table 5. However, no noticeable change of the leakage flow rate is shown as the area in the shroud leakage path is increased from  $A1 (102 \, \text{mm}^2)$  to  $A3 (408 \, \text{mm}^2)$ .

3.2.5 Effect of Seal Clearance. This section investigates the effect of the wear ring, end-seal clearance on impedances. The selected seal clearances for the comparison are 0.36, 0.54, and 0.7 mm. The imposed boundary conditions for the simulations are assumed to be the same for all cases. The computed results are

wnloaded from http://asmedigitalcollection.asme.org/vibrationacoustics/article-pdf/138/3/031014/6346637/vib\_138\_03\_031014.pdf?casa\_token=orjJsTrijzQAAAAA:Yg0eBEhCe4a=Eu3llHAao-0\VZAetusZxDnEVhlABx2Vx89oRoV9qemrUG1\_C-U2w0xMnUb by Texas A & M University user on 08 August 20

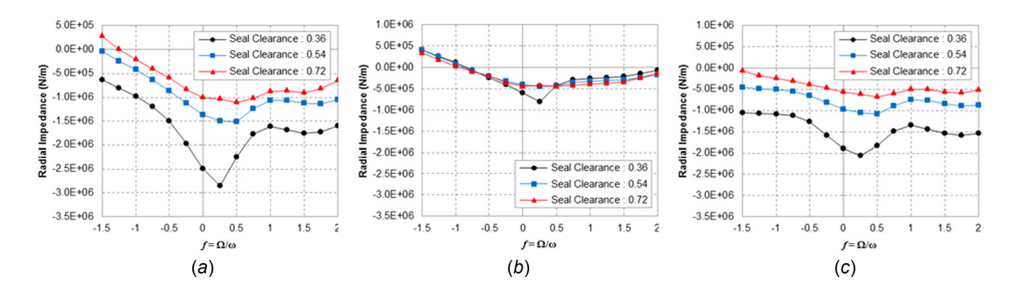


Fig. 18 Radial impedances for the wear-ring seal impeller according to the seal clearance (a) combined (shroud + seal), (b) shroud, and (c) seal

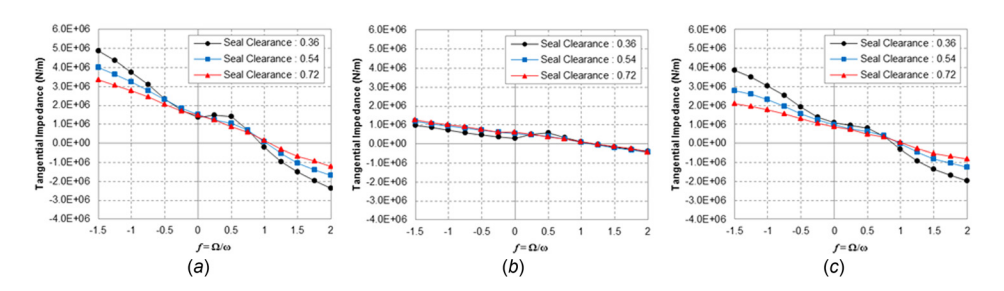


Fig. 19 Tangential impedances for the wear-ring seal impeller according to the seal clearance (a) combined (shroud + seal), (b) shroud, and (c) seal

Table 6 Comparison of leakage flow rate according to the seal clearance

	Seal clearance			
	0.36	0.54	0.72	
Leakage (kg/s)	3.5685	6.6498	9.5105	

described in Figs. 18 and 19. Like the previous cases in this paper, the shroud has a relatively larger contribution as a cause for the bump and dip in the impedance curves. In case of 0.36 mm, the phenomenon can be seen clearly and the peaks disappear with the increased seal clearance as shown in Figs. 18(b) and 19(b). The y-intercepts of the radial and tangential impedances in Figs. 18(c) and 19(c) decrease when the seal clearance is increasing. If assumed that the impedances are approximately modeled using Eq. (1), the decreased y-intercepts in impedance curves imply reduced direct stiffness and cross-coupled stiffness, respectively. The same trend was predicted for the conventional wear-ring seal impeller by the bulk flow analysis of Childs [7]. Table 6 indicates the leakage flow rate increases more than proportionately as the wear-ring seal clearance increase.

#### 4 Summary and Conclusions

The fluid-induced forces arising in the leakage flow path of the shrouded centrifugal impeller have been investigated utilizing the CFD approach. ANSYS CFX is employed to predict the rotordynamic forces caused by a whirling centrifugal impeller. The computational approach is verified by reasonable prediction of the rotordynamic coefficients for the face-seal impeller as compared with other approaches and experiment. A wide range of WFRs (-1.5-2.0) are considered to check the existence of the bump and dip in the impedance curves of the face-seal impeller case. The conventional quadratic least square curve-fit approach can be used to determine the rotordynamic coefficients of the face-seal impeller since there are no significant bump and dip in the impedance curves.

A conventional wear-ring seal impeller is analyzed and the radial and tangential impedances are computed. The results of the simulation show peaks in the impedances which have not been observed in the prior CFD models, but have appeared in the bulk flow impeller analysis of Childs. Review of past experimental work also shows the peaks in measured impeller impedances. ISR, flow rate of primary passage, shape of shroud, and seal clearance are varied to analyze their effects in the conventional wear-ring seal impeller impedances. Numerical calculations for the various case studies are implemented by varying the selected parameters for the wear-ring seal impeller and the following conclusions are

- (a) The impedances from the seal are relatively larger than the values from the shroud of the conventional wear-ring seal impeller. The bump and dip in the impedance curves of the impeller are caused mainly by forces originating in the shroud rather than the seal. The phenomenon is clearly observed in the tangential impedance. The bump and dip in the predicted impedance curves increase with higher ISR.
- (b) The wear-ring seal impeller is less destabilizing and the size of the impedance peaks decrease at higher flow rate of the primary passage. The trend is identical to the results of the experiment by Franz and Arndt [13].
- (c) Added recirculation zones in the leakage flow path reduce the velocity of the circumferential direction in the shroud surface and the magnitude of the impedance peaks. With larger added area in the shroud leakage path, the peaks in the impedance curves can be suppressed more effectively. Leakage flow rate is reduced with the additional recirculation zone.
- (d) Enlarging the seal clearance of the impeller is one method to reduce the size of the dip and bump. However, using a larger clearance seal in the impeller model has the negative effect of increasing the leakage flow rate.

# Acknowledgment

The authors would like to thank the Texas A&M Turbomachinery Research Consortium (TRC) member companies for funding this research. The authors also acknowledge the Texas A&M

Supercomputing Facility<sup>1</sup> for providing computing resources useful in conducting the research reported in this paper.

# Nomenclature

 $f = \text{whirl frequency ratio: } \Omega/\omega$ 

 $F_r$ ,  $F_t$  = radial and tangential reaction force (N)

k = turbulence kinetic energy

k, c, m =cross-coupled stiffness, damping, mass (N/m, N s/m, kg)

K, C, M =direct stiffness, damping, mass (N/m, N s/m, kg)

p = static pressure

 $V_0$  = inlet tangential velocity

x, y, z = Cartesian coordinates

 $\varepsilon$  = whirling orbit radius (m)

 $\varepsilon = epsilon$ 

 $\omega = \text{spin speed (rad/s)}$ 

 $\Omega$  = whirl speed (rad/s)

 $\Omega_w$  = whirl frequency ratio at instability

# References

- [1] Jery, B., Acosta, A. J., Brennen, C. E., and Caughey, T. K., 1984, "Hydrodynamic Impeller Stiffness, Damping, and Inertia in the Rotordynamics "Hydrodynamic Impelier Stiffness, Damping, and metita in the Roccaymanneo of Centrifugal Flow Pumps," Rotordynamic Instability Problems in High Performance Turbomachinery: Proceedings of a Workshop Held at Texas A&M University, May 28–30, NASA Report No. CP2338, pp. 137–160.
- [2] Bolleter, U., Wyss, A., Welte, I., and Sturchler, R., 1987, "Measurement of Hydrodynamic Interaction Matrices of Boiler Feed Pump Impellers," J. Vib.,
- Stress, Reliab. Des., 109(2), pp. 144–151.
  [3] Bolleter, U., Leibundgut, E., Sturchler, R., and McCloskey, T., 1989, "Hydraulic Interaction and Excitation Forces of High Head Pump Impellers," Pumping Machinery: Third Joint ASCE/ASME Mechanics Conference, La Jolla, CA, July 9-12, pp. 187-194.
- [4] Ohashi, H., Sakuraki, A., and Nishikoma, J., 1988, "Influence of Impeller and Diffuser Geometries on the Lateral Fluid Forces of Whirling Centrifugal Impeller," Rotordynamic Instability Problems in High Performance Turbomachinery:

- Proceedings of a Workshop Held at Texas A&M University, NASA, Washington
- DC, NASA Report No. CP3026, pp. 285–306. Yoshida, Y., and Tsujimoto, Y., 1990, "An Experimental Study of Fluid Forces on a Centrifugal Impeller Rotating and Whirling in a Volute Casing," Third International Symposium on Transport Phenomena and Dynamics of Rotating
- Machinerry (ISROMAC-3), Honolulu, HI, Apr. 1-4, Vol. 2, pp. 483–506. Tsujimoto, Y., Yoshida, Y., Ohashi, H., Teramoto, N., and Ishizaki, S., 1997, 'Fluid Force Moment on a Centrifugal Impeller Shroud in Precessing Motion," ASME J. Fluids Eng., 119(2), pp. 366-371.
- [7] Childs, D., 1989, "Fluid-Structure Interaction Forces at Pump Impeller-Shroud Surfaces for Rotordynamic Calculations," ASME J. Vib., Acoust., Stress, Reliab. Des., 111(3), pp. 216-225
- [8] Baskharone, E. A., Daniel, A. S., and Hensel, S. J., 1994, "Rotordynamic Effects of the Shroud-to-Housing Leakage Flow in Centrifugal Pumps," ASME J. Fluids Eng., 116(3), pp. 558–563.
- [9] Baskharone, E. A., and Wyman, N. J., 1999, "Primary/Leakage Flow Interaction in a Pump Stage," ASME J. Fluids Eng., 121(1), pp. 133–138.

  [10] Moore, J. J., and Palazzolo, A. B., 2001, "Rotordynamic Force Prediction of
- Whirling Centrifugal Impeller Shroud Passages Using Computational Fluid Dynamic Techniques," ASME J. Eng. Gas Turbines Power, 123(4), pp. 910-918.
- [11] Gupta, M. K., and Childs, D., 2010, "Rotordynamic Stability Predictions for Centrifugal Compressors Using a Bulk-Flow Model to Predict Impeller Shroud Force and Moment Coefficients," ASME J. Eng. Gas Turbines Power, 132(9), p. 091402.
- [12] Moore, J. J., Ransome, D. L., and Viana, F., 2011, "Rotordynamic Force Prediction of Centrifugal Compressor Impellers Using Computational Fluid Dynamics," ASME J. Eng. Gas Turbines Power, 133(4), p. 042504.
- [13] Franz, R., and Arndt, N., 1986, "Measurement of Hydrodynamic Forces on the Impeller of HPOTP of the SSME," California Institute of Technology, Pasadena, CA, Report No. E249.2.
- [14] Brennen, C. E., Franz, R., and Arndt, N., 1988, "Effects of Cavitation on Rotor-dynamic Force Matrices," 3rd Conference on Advanced Earth-to Orbit Propulsion Technology, Huntsville, AL, May 10-12, NASA, Washington, DC, pp.
- [15] ANSYS, 2010, CFX-Solver Theory Guide, release 13.0, Ansys Inc., Canonsburg, PA
- [16] Moore, J. J., and Palazzolo, A. B., 1999, "CFD Comparison to 3D Laser Anemometer and Rotordynamic Force Measurements for Grooved Liquid Annular Seals," ASME J. Tribol., 121(2), pp. 306-314.
- [17] Untaroiu, A., Untaroiu, C. D., Wood, H. G., and Allaire, P. E., 2013, 'Numerical Modelling of Fluid-Induced Rotordynamic Forces in Seals With Large Aspect Ratios," ASME J. Eng. Gas Turbines Power, 135(1), p. 012501.

<sup>1(</sup>http://sc.tamu.edu/)